Mapping mantle flow during retreating subduction: Laboratory models analyzed by feature tracking

F. Funiciello,[1] M. Moroni,[2] C. Piromallo,[3] C. Faccenna,[1] A. Cenedese,[2] and H. A. Bui[1]

Received 20 April 2005; revised 14 November 2005; accepted 21 November 2005; published 2 March 2006.

[1] Three-dimensional dynamically consistent laboratory models are carried out to model the large-scale mantle circulation induced by subduction of a laterally migrating slab. A laboratory analogue of a slab–upper mantle system is set up with two linearly viscous layers of silicone putty and glucose syrup in a tank. The circulation pattern is continuously monitored and quantitatively estimated using a feature tracking image analysis technique. The effects of plate width and mantle viscosity/density on mantle circulation are systematically considered. The experiments show that rollback subduction generates a complex three-dimensional time-dependent mantle circulation pattern characterized by the presence of two distinct components: the poloidal and the toroidal circulation. The poloidal component is the answer to the viscous coupling between the slab motion and the mantle, while the toroidal one is produced by lateral slab migration. Spatial and temporal features of mantle circulation are carefully analyzed. These models show that (1) poloidal and toroidal mantle circulation are both active since the beginning of the subduction process, (2) mantle circulation is intermittent, (3) plate width affects the velocity and the dimension of subduction induced mantle circulation area, and (4) mantle flow in subduction zones cannot be correctly described by models assuming a two-dimensional steady state process. We show that the intermittent toroidal component of mantle circulation, missed in those models, plays a crucial role in modifying the geometry and the efficiency of the poloidal component.

Citation: Funiciello, F., M. Moroni, C. Piromallo, C. Faccenna, A. Cenedese, and H. A. Bui (2006), Mapping mantle flow during retreating subduction: Laboratory models analyzed by feature tracking, *J. Geophys. Res.*, *111*, B03402, doi:10.1029/2005JB003792.

1. Introduction

[2] Subduction is the fundamental and most studied process in modern geodynamics; yet many aspects are not well understood in all details. One example is represented by the secondary flow triggered in the mantle by subduction, still unclear despite its crucial role in controlling and influencing many important processes active in the subduction factory, such as the path of melt from the source region and the distribution of geochemical anomalies.

[3] Seismological observations have provided progressively more detailed constraints on mantle circulation in subduction zones. The most straightforward indication is offered by earthquake hypocenters associated with Benioff zones [*Isacks and Barazangi*, 1977; *Giardini and Woodhouse*, 1984; *Grand et al.*, 1997], representing trajectories of descending lithosphere. Another evidence for the pattern of flow in the mantle comes from shear wave splitting studies [*Silver and Chan*, 1991; *Savage*, 1999; *Fischer et al.*, 2000; *Iidaka and Niu*, 2001; *Barruol and Granet*, 2002; *Nakajima and Hasegawa*, 2004] and azimuthal seismic anisotropy from surface waves inversions (see *Montagner and Guillot* [2000] for a thorough review). Assuming that mantle anisotropy is due to lattice-preferred orientation of olivine crystals in the shear strain field associated with the flow of material, the direction of fast shear wave velocities can provide important information about mantle flow at lithospheric and asthenospheric depths [*Ben Ismail and Mainprice*, 1998]. Seismological observations give short-term images of mantle flow, while long-term circulation is generally much harder to define. Geochemical, isotopic and petrologic signatures [*Wendt et al.*, 1997; *Turner and Hawkesworth*, 1998; *Pearce et al.*, 2001] give indirect constrains on rates and direction of mantle flow. On the other hand, only analytical, numerical and laboratory models are able to provide and test mechanisms and evolutionary scenarios for mantle flow in subduction zones.

[4] Flow in subduction zones is frequently conceptualized in terms of a two-dimensional (2-D) corner flow driven by shear coupling to the downgoing slab [*Tovish et al.*, 1978]. In this regard, 2-D numerical models study mantle flow produced by kinematically imposed subduction velocity along a fixed direction (i.e., longitudinal subduction). Related results range from the description of a simple advective flow [*Turcotte and Schubert*, 1982] to more complex solutions taking into account thermal and compo-

[1]Dipartimento di Scienze Geologiche, Università degli Studi "Roma TRE," Rome, Italy.
[2]Dipartimento di Idraulica, Trasporti e Strade, Università degli Studi di Roma "La Sapienza," Rome, Italy.
[3]Istituto Nazionale di Geofisica e Vulcanologia, Rome, Italy.

0148-0227/06/2005JB003792$09.00

sitional evolution produced by mantle circulation [*Davies and Stevenson*, 1992; *Conder et al.*, 2002; *Eberle et al.*, 2002] also in presence of a moving overriding plate [*Fischer et al.*, 2000]. This approach leads to twofold problems. The first issue concerns the simplified use of a longitudinal subduction. Lateral slab migration cannot be ignored since most subduction zones are advancing or retreating [*Heuret and Lallemand*, 2004] and able to induce geometrically complex mantle circulation as first demonstrated by *Garfunkel et al.* [1986], though in 2-D only. Migrating slabs do not separate convection cells as specified by the corner flow theory, instead they take part in the convection process, their dip forming an angle with mantle streamlines. Hence lateral slab migration allows the displacement of material away from one side and inward flow of an equal volume toward the other side [*Garfunkel et al.*, 1986; *Kincaid and Sacks*, 1997; *Olbertz et al.*, 1997]. In terms of thermal evolution this implies a warmer slab surface temperature [*Kincaid and Sacks*, 1997] and enhances decompression melting [*Kincaid and Hall*, 2003]. As a second problematic question, the 2-D approximation is inappropriate to describe subduction zones, which are complex three-dimensional (3-D) structures [*Jarrard*, 1986]. Models based on corner flow approach do not properly reconcile all geophysical observables. For instance, mantle circulation pattern recognized by anisotropy studies is unpredictable using simplified 2-D subduction models, thus invoking interpretations which consider 3-D aspects, as extension in back-arc basins [*Yang et al.*, 1995], slab rollback and escape of the underlying mantle as suggested for the Andes [*Russo and Silver*, 1994], mantle circulation inside slab windows, as for the Tyrrhenian [*Faccenna et al.*, 2004], Kamchatka [*Peyton et al.*, 2001], or mantle circulation around slab edges as for Tonga [*Smith et al.*, 2001].

[5] The 3-D numerical models of subduction are not yet producing satisfactory results in predicting long-term subduction due to still limited available computational capacities. Even if an initial 3-D geometry can be maintained in models with Newtonian rheology [*Zhong et al.*, 1998], the long-term subduction results in unrealistic two-sided symmetrical subduction [*Tackley*, 2000b, 2000a].

[6] Laboratory experiments are intrinsically 3-D. However, 3-D aspects are often suppressed using laterally homogeneous slabs controlled by confined box boundary [*Kincaid and Olson*, 1987; *Shemenda*, 1992] or by using 2-D feeding pipes to inject the slab into a fluid of lower viscosity/density [*Griffiths and Turner*, 1988; *Griffiths et al.*, 1995; *Guillou-Frottier et al.*, 1995]. The 3-D laboratory models accounting for lateral slab migration have been realized kinematically by *Buttles and Olson* [1998] and dynamically by *Funiciello et al.* [2003, 2004] and *Schellart*, [2004b, 2004a]. These models provide qualitative insights into mantle circulation in response to lithospheric subduction. A big step forward has been recently done by *Kincaid and Griffiths* [2003, 2004] through a series of 3-D laboratory experiments aimed at quantitatively studying mantle flow generated by subduction and the consequent temperature variations in the slab and overlying mantle wedge. Their results show that the style of plate sinking affects the subduction process in terms of orientation, speed, and temperature of the induced mantle circulation and temperature at the surface of the subducting lithosphere. Despite the importance of these models, the first examples of simulating a T-dependent 3-D slab mantle, the applicability of their results to natural cases can be strongly limited by their "a priori" imposition of subduction and trench motion.

[7] The goal of the present study is to provide new insights on mantle circulation in subduction zones as inferred by 3-D laboratory models. Our models have the advantage of carrying out a self-consistent subduction, in which the circulation triggered in the mantle by subduction is created and interacts with the system dynamics. In particular, the role of the subducting plate width and lithosphere-mantle density/viscosity ratios on mantle circulation is systematically considered. Models are built upon our previous efforts [*Funiciello et al.*, 2003, 2004; *Bellahsen et al.*, 2005] by adding a new sophisticated apparatus able to continuously monitor and to quantitatively estimate the 3-D velocity field and mantle flow pattern by using a nonintrusive particle image analysis technique. We have built up a set of codes to appropriately postprocess data provided by the image analysis algorithm.

[8] Over the past few decades particle imaging based techniques have been extensively used in engineering studies to obtain multipoint velocity measurements [*Boffetta et al.*, 2000; *Moroni and Cushman*, 2001; *Di Florio et al.*, 2002]. Only recently the application of particle imaging techniques has been extended to geodynamic laboratory models: Particle Image Velocimetry (PIV [*Adrian*, 1991; *Nogueira et al.*, 2001]) has been used to reconstruct 2-D Eulerian velocity/displacement fields of deforming systems [*Adam et al.*, 2002; *Hampel et al.*, 2003] and to investigate laboratory flow produced by convection/advection processes [*Davaille et al.*, 2003; *Kincaid and Griffiths*, 2003; *Kincaid and Hall*, 2003; *Kumagai et al.*, 2003; *Kincaid and Griffiths*, 2004]. This paper presents the application of a Feature Tracking (FT) technique [*Miozzi*, 2004; *Moroni and Cenedese*, 2006], which allows a Lagrangian description of the velocity field providing sparse velocity vectors with application points coincident with large luminosity intensity gradients (likely located along tracer particles boundaries). Lagrangian data are then used to reconstruct instantaneous and time-averaged Eulerian velocity fields through a resampling procedure. FT compared to PIV allows a larger spatial resolution (being able to detect regions closer to the box boundaries) and an increased dynamic range [*Moroni and Cenedese*, 2006]. Further, providing trajectories instead of velocity field, it allows understanding and qualitatively detecting flow characteristics much easier than PIV. If compared to other tracking algorithms, FT is not constrained by low seeding density, so it provides accurate displacement vectors even when the number of tracer particles within each image is very large. In particular, our FT system simultaneously measures the 2-D displacement fields within two planes properly acquired by the recording system. The information gathered by the two cameras is then combined to study the 3-D mantle circulation induced by subduction.

[9] These experiments show that a retreating slab creates a complex 3-D time-dependent mantle circulation pattern characterized by the simultaneous presence of the poloidal and toroidal flow components since the beginning of the subduction process. Spatial and temporal features of mantle

circulation are carefully described highlighting its intermittent behavior. In particular, we find that mantle flow produced by 3-D dynamically consistent laboratory experiments of subduction is considerably different compared to 2-D corner flow theory models. Hence we emphasize that models and consequent natural implications descending from 2-D studies cannot be considered accurate.

2. Experimental Setup

2.1. Assumptions

[10] Assumptions underlying the setup of our models are listed in sections (for more detailed explanations, see *Funiciello et al.* [2003, 2004]).

2.1.1. Viscous Rheology

[11] Similarly to what already done in our previous experiments [*Faccenna et al.*, 1999; *Funiciello et al.*, 2003, 2004; *Bellahsen et al.*, 2005], we simulate the Earth system using linearly viscous rheologies.

2.1.2. Self-Consistent Subduction

[12] Slab pull is the only active force within the system. No external kinematic boundary conditions, such as plate or trench velocity, are applied. This ensures that the experimental subduction process is a self-consistent response to the dynamic interaction between the slab and the mantle.

2.1.3. Convectively Neutral Mantle

[13] We are interested in isolating the effect of advection inside the mantle produced by the subducting slab. Hence, in our experiments flow is generated only by subduction. We neglect thermal convection as well as the effect of global [*Ricard et al.*, 1991] or local background flow that is not generated by the plate/slab system.

2.1.4. Isothermal Experiments

[14] Experimental limitations lead us to neglect thermal effects during the subduction process. Hence we assume constant chemical density contrast throughout the experiment, and the role of thermal diffusion and phase changes [*Bunge et al.*, 1997; *Lithgow-Bertelloni and Richards*, 1998; *Tetzlaff and Schmeling*, 2000] is neglected. In this view the slab is thought to be in a quasi-adiabatic state. The high subduction velocity (larger than 1 cm/yr in nature) recorded in our experiments justifies this assumption, ensuring that advection overcomes conduction [*Wortel*, 1982; *Bunge et al.*, 1997].

[15] It is impossible to reproduce in laboratory the fundamental role of the endothermic phase change at the transition zone. Therefore the barrier to direct slab penetration into the lower mantle is simulated by the increase of viscosity with depth, for the limited timescale of the analyzed process [*Davies*, 1995; *Guillou-Frottier et al.*, 1995; *Christensen*, 1996; *Funiciello et al.*, 2003]. In particular, we assume the bottom of the box as analogue of the 660 km discontinuity.

2.1.5. No Overriding Plate

[16] The overriding plate is not modeled. Hence we have a free-slip top boundary and we assume that the fault zone between the subducting and the overriding plates is weak, having the same viscosity of the upper mantle [*Tichelaar and Ruff*, 1993; *Zhong and Gurnis*, 1994; *Conrad and Hager*, 1999]. We assume as well that the overriding plate passively moves with the retreating trench. This choice does not invalidate the general behavior of the experimental results but may influence the rate of the subduction process [*King and Hager*, 1990] and mantle circulation.

2.2. Materials

[17] We use silicone putty (Rhodrosil Gomme, PBDMS + iron fillers) and glucose syrup as analogue of the lithosphere and upper mantle, respectively. Silicone putty is a viscoelastic material with purely viscous behavior at experimental strain rates [*Weijermars and Schmeling*, 1986], whose timescale is larger than the Maxwell relaxation time (about 1 s). Glucose syrup is a transparent Newtonian low-viscosity and high-density fluid. These materials have been selected to achieve the standard scaling procedure for stresses scaled down for length, density and viscosity in a natural gravity field ($g_{model} = g_{nature}$) as described by *Weijermars and Schmeling* [1986] and *Davy and Cobbold* [1991].

[18] Scale factor for length is 1.6×10^{-7} (1 cm in the experiment corresponds to 60 km). Densities and viscosities are assumed as constant over the thickness of the individual layers considering them as an average of effective values. The scale density factor between the oceanic lithosphere and the upper mantle ranges between 1.05 and 1.07 [*Molnar and Gray*, 1979; *Cloos*, 1993]. The viscosity ratio between the slab (η_l) and the upper mantle (η_{um}) ranges between 10^4 and 10^5 Pa s. This is an upper limit for viscosity; therefore the subduction rates of the experiments have to be considered as an upper bound. The influence of a large range of viscosity contrasts on the subduction induced flow has been studied by means of numerical instantaneous flow models and is extensively discussed by C. Piromallo et al. (Three-dimensional instantaneous mantle flow induced by subduction, submitted to *Geophysical Research Letters*, 2005). Considering the imposed scale ratio for length, gravity, viscosity and density (Table 1) applied to the lithosphere, 1 Myr in nature corresponds to ~1 min in the experiments. Parameters and values for nature and the experimental system are listed in Table 1.

2.3. Experimental Procedure

2.3.1. Subducting System

[19] The layered system is arranged in a transparent Plexiglas tank of square horizontal cross section ($80 \times 80 \times 20$ cm^3) (Figure 1). Glucose syrup is previously seeded with neutrally buoyant, highly reflecting air microbubbles ($\ll$1 mm diameter) used as passive tracers to map flow circulation patterns using a FT technique. These tracers negligibly influence density and viscosity of the mantle fluid.

[20] Since the experiments are designed to map the 3-D mantle flow induced by the subduction process, it is important to avoid any box boundary effect that could alter the final results. Hence we follow the procedure already adopted by *Funiciello et al.* [2004] allowing a distance as large as possible between the plate and box sides (>20–30 cm) to minimize the lateral box boundaries effects.

[21] In each experiment the plate is free to move as a self consistent response to subduction dynamics ("free ridge" in the sense of *Kincaid and Olson* [1987]). Therefore we assume that plates are completely surrounded by fault zones (trench and transform faults) whose equivalent viscosity is the same as the upper mantle. These conditions result in a

Table 1. Scaling of Parameters in Nature and in Laboratory[a]

Parameter	Nature	Models 1, 2, 3	Models 4, 5, 6
Gravitational acceleration g, m s^{-2}	9.8	9.8	9.8
Thickness			
Oceanic lithosphere h, m	100,000	0.016	0.016
Upper mantle H, m	660,000	0.11	0.11
Scale factor for length ($L_{model}/L_{nature} = 1.6 \times 10^{-7}$)			
Density			
Oceanic lithosphere ρ_l, kg m^{-3}	3,300	1480	1480
Upper mantle ρ_{um}, kg m^{-3}	3,220	1415	1382
Density contrast ($\rho_l - \rho_{um}$)	80	65	98
Density ratio (ρ_l/ρ_{um})	1.02	1.05	1.07
Viscosity			
Oceanic lithosphere η_l, Pa s	10^{24}	3.6×10^5 (±5%)	3.6×10^5(±5%)
Upper mantle η_{um}, Pa s	10^{19}–10^{20}	30 (±20%)	3 (±20%)
Viscosity ratio (η_l/η_{um})	10^4–10^5	$\sim 10^4$	$\sim 10^5$
Characteristic time t, s (t_{nature}/t_{model} = $(\Delta\rho g h)_{lith\ model}/(\Delta\rho g h)_{lith\ nature}$ ($\eta_{l\ nature}/\eta_{l\ model}$))	3.1×10^{13} (1 Myr)	~60 (~1 min)	~60 (~1 min)

[a]If models 4, 5, and 6 are scaled for mantle, 1 Myr in nature is equal to about 5 s in laboratory.

higher velocity [*King and Hager*, 1994] but ensure the maximum mobility of the plate.

[22] The subduction process is manually started in all the experiments by forcing downward the leading edge of the silicone plate into the glucose to a depth of 3 cm (corresponding to about 180 km in nature) and with an angle of ~30°.

[23] A total number of 40 different experiments are performed systematically while changing the plate width and mantle viscosity and density. Experiments are performed at least twice to ensure reproducibility. In Table 2 we summarized the characteristics of the selected experiments we describe in the present paper.

2.3.2. Monitoring System

[24] Each experiment is monitored over its entire duration by two black and white progressive scan cameras imaging the lateral and top views (Figure 1). Trench retreat, dip of the slab, and mantle circulation pattern are measured.

[25] As far as it concerns the analysis of mantle circulation, a good compromise between pixel resolution and

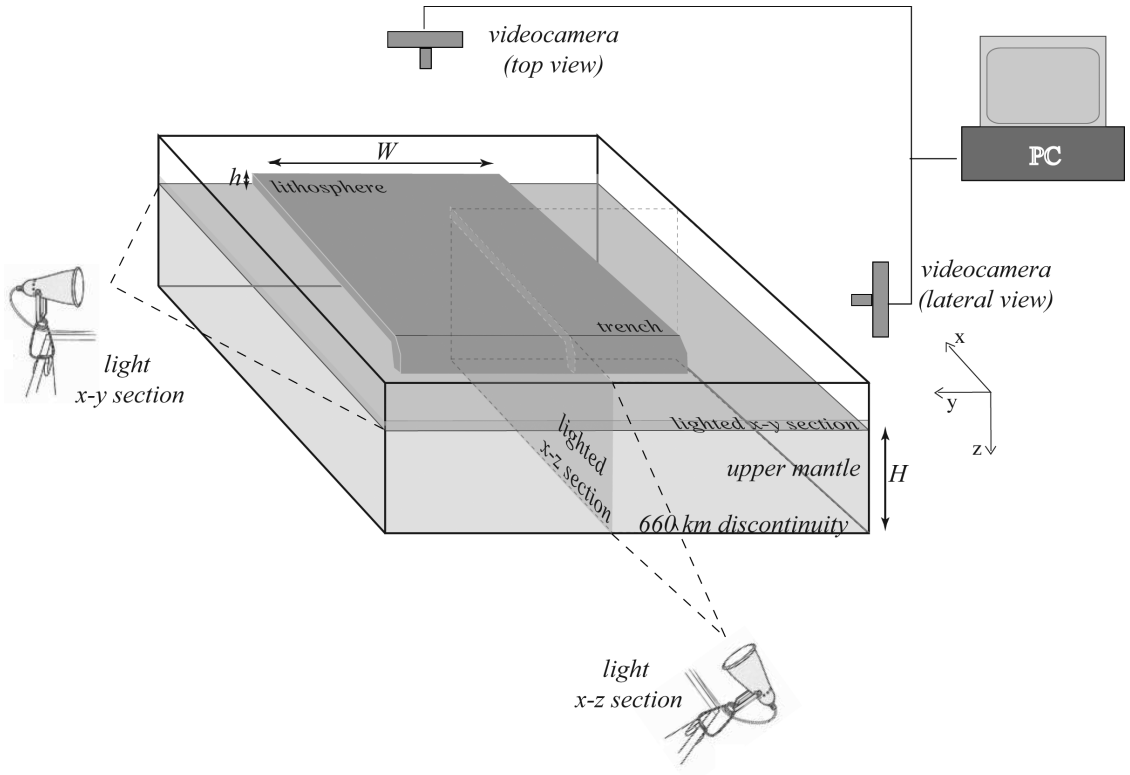

Figure 1. Experimental setup. The lithosphere is simulated by means of a silicone plate of density ρ_l, viscosity η_l, width w, thickness h, and length L. The mantle is simulated by means of glucose syrup of density ρ_m, viscosity η_m, and thickness H. Experiments are monitored over their entire duration in the lateral and top view by two black and white cameras (25 frames s^{-1}) framing the two lighted sections.

Table 2. Description of the Materials and Parameters Used in the Selected Experiments

Experiment	h_l, m	w, m	ρ_l, kg m^{-3}	ρ_{um}, kg m^{-3}	η_l, Pa s	η_{um}, Pa s
1	0.016	0.3	1480	1415	3.6×10^5	30
2	0.016	0.2	1480	1415	3.6×10^5	30
3	0.016	0.1	1480	1415	3.6×10^5	30
4	0.011	0.3	1480	1382	3.6×10^5	3
5	0.016	0.2	1480	1382	3.6×10^5	3
6	0.016	0.1	1480	1382	3.6×10^5	3

dimension of the investigated area is obtained by assuming mirror symmetry of flow along the plate centerline and by framing with the top view camera a window roughly centered at the trench (Figure 1). Two neon lights (36 W power) produce a planar uniform radiation focused onto two normal cross sections through the system: the *x*-*z* plane through the centerline of the tank-slab system and the *x*-*y* plane just below the plate at a depth of about 150 km (Figure 1). The thickness of the light sheet is about 5 mm. Images of the bright reflecting microbubbles used as passive tracer particles are recorded by the two cameras, set to acquire 25 frames per second. The selected imaging rate optimizes the time resolution of the method. Movies are then stored on the hard disk of a dedicated laptop and postprocessed using a FT image-processing technique (see section 3 for details) to retrieve the circulation pattern. As a final result we obtain the trajectory of each single tracer particle within the two lighted orthogonal interrogation windows it belongs to for the whole duration of experiments.

[26] Kinematic and geometric parameters (trench retreat, dip of the slab, mantle velocity field, mantle velocity *x* and *y* components and modulus, streamlines of mantle circulation, mantle linear flux) are afterward quantified by means of data analysis tools. To allow an easier comparison between experimental results and natural cases, we express mantle velocity in terms of percentage of trench velocity.

3. Image Analysis Technique

3.1. Feature Tracking

[27] FT is an image analysis technique well-known in Computer Vision but still not widely used for fluid dynamics applications. FT algorithms focus their attention on pixel luminosity intensity gradients distributed within each image. Recalling the ''image brightness constancy constraint'' and assuming the hypothesis of tracer particles behaving as Lambertian surfaces (their luminosity values do not depend on the point of view of the observer), the total derivative of the luminosity intensity, I, is equal to zero:

$$\frac{DI}{Dt} = \frac{\partial I}{\partial t} + u\frac{\partial I}{\partial x} + v\frac{\partial I}{\partial y} = \frac{\partial I}{\partial t} + \nabla I^T \cdot \mathbf{U} = I_t + uI_x + vI_y = 0 \tag{1}$$

where

$$\nabla I(\mathbf{x}, t) = \begin{bmatrix} \dfrac{\partial I(\mathbf{x}, t)}{\partial x} \\ \dfrac{\partial I(\mathbf{x}, t)}{\partial y} \end{bmatrix} = \begin{bmatrix} I_x \\ I_y \end{bmatrix} \tag{2}$$

Equation (1) states that local variations in the intensity are balanced by convective changes. $I(x, y, t)$, function of the position (x, y) and time t, is known within each image.

[28] Equation (1) contains two unknowns, u and v (which are the velocity components), and can be solved only under some constraints. The solution of (1) will provide the velocity vector components with application point coincident with the position (x, y) where the equation is solved. To have enough constraints to solve equation (1), it has to be applied to a window W centered at (x, y). In other words, given the image acquired at time t, choosing a point of coordinates (x, y) and building a window of given size around it, FT looks for the most similar window of the same size in the image acquired at time $t + \Delta t$. In particular, the quantity ε_w, also defined as sum of squared differences (SSD) among intensity values, function of W, represents the difference of the intensity values between the image at time t and the image at time $t + \Delta t$. The problem is then reformulated as a minimization in a least squares sense where the function ε_w is differentiated respect to the displacement vector U, providing a system with two equations and two unknowns. The solution of the whole procedure is a velocity vector that better approximates the motion of the interrogation window W.

[29] The most interesting characteristic of FT is that the existence of a solution for the system depends on where the solution is looked for. In other words, it is possible to monitor the solution accuracy which depends on spatial derivatives of the image luminosity in both directions computed in the location where the system is solved. In short, the FT algorithm defines implicitly the features, i.e., (x, y) coordinate pairs, that are good to track. As a tracking technique, FT performances may be compared to classical Particle Tracking Velocimetry (PTV). As an image analysis technique, it may be compared to Particle Image Velocimetry (PIV). While FT does not require the input of any parameter somehow related to the flow field features, classical PTV algorithms need the input of two parameters related to the maximum velocity and to the acceleration within the flow field. Tracking of particles is then performed constraining the search of the same particle at subsequent times within limits described by the two parameters above. To increase the accuracy of the trajectories reconstructed with PTV, the seeding density has to be low. Both PIV and FT use interrogation windows (inner product of intensity values for the former and a distance measure, SSD, for the latter), but PIV identifies the higher peak within the correlation matrix while FT solves a minimization problem. While PIV subdivides the flow domain into a grid of fixed dimensions and solves the velocity field at the grid nodes, FT is a more flexible technique providing the velocity vector at each location where a significant intensity gradient exists, i.e., where a good feature to track does exist.

3.2. Resampling Algorithm

[30] In general, all particle tracking procedures yield a number of trajectories from which two velocity components can be computed. It may be advantageous to interpolate this data to a regular grid. The following algorithm accomplishes this:

[31] 1. Overlap a M rows and N columns grid to the acquired field.

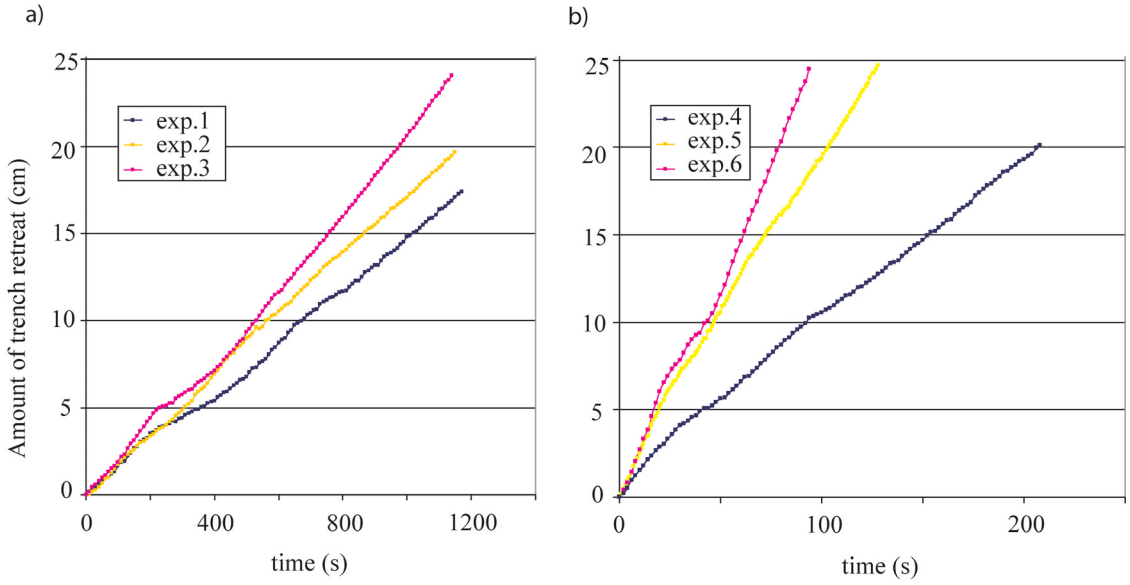

Figure 2. Trench motion versus time for experiments (a) 1, 2, 3 and (b) 4, 5, 6. The tangent to every point of the curves corresponds to v_t.

[32] 2. Introduce two quantities q_x and q_y, where q_x is the ratio of the horizontal resolution (720 pixels in our case) to the number of columns and q_y is the ratio of the vertical resolution (576 pixels in our case) to the number of rows.

[33] 3. Compute the x axis and y axis coordinates of the grid nodes (in pixel) $((x_k, y_r)$; $k = 1{:}N$, $r = 1{:}M)$.

[34] 4. Compute a set of three matrices for each repetition of the experiment: (1) the matrix containing the number of velocity samples belonging to the cell of coordinates x_k and y_r (N); and (2) the matrices containing the mean longitudinal and transverse velocity $(\overline{U}, \overline{V})$ obtained by averaging over all the velocity samples belonging to the cell. Different averaging methods can be employed: arithmetic, Gaussian, inverse distance and adaptive Gaussian arithmetic average to mention a few. The general resampling algorithm for the longitudinal component (the algorithm for the transverse component is analogous) is

$$\overline{U}(i,j) = \frac{1}{\mathrm{NORM}}\Theta(u_k) \tag{3}$$

where Θ is a general operator corresponding to the Gaussian average in our case:

$$\sum_{k=1}^{N(i,j)} u_k \exp\left\{-\left[(x_k - x_j)^2 + (y_k - y_i)^2\right]/\sigma^2\right\} \tag{4}$$

and NORM is a normalization parameter to be specialized according to the averaging procedure:

$$\sum_{k=1}^{N(i,j)} \exp\left\{-\left[(x_k - x_j)^2 + (y_k - y_i)^2\right]/\sigma^2\right\} \tag{5}$$

As a result, time-averaged velocity fields are obtained on a regular grid. From these data velocity fields are processed to obtain velocity maps (modulus, x-y components, streamlines).

4. Experimental Results

[35] Our experiments are designed to provide new insights on mantle flow in subduction zones as inferred by 3-D dynamically self-consistent laboratory models. Similar experiments have already been performed by *Funiciello et al.* [2003, 2004] and *Bellahsen et al.* [2005]. These works have shown that the geometry and behavior of the subduction zone can significantly vary using combinations of thickness, viscosities and densities of the plate and the mantle [*Bellahsen et al.*, 2005] and depending on the lateral boundary conditions ("laterally constrained" or "laterally unconstrained" configuration [*Funiciello et al.*, 2004]). The novelty of this work resides in that, introducing a new monitoring analysis apparatus, we are able for the first time to quantify the spatial and the temporal evolution of the mantle circulation induced by subduction. Velocity fields are obtained on a regular grid and are lately processed to obtain velocity maps that we use to describe the mantle circulation.

[36] In particular, the role of subducting plate width and mantle viscosity/density is considered. We present a selection of 6 out of 40 experiments, first showing the subduction of a 20 cm wide oceanic plate (corresponding to 1200 km in nature) in a mantle with 10 Pa s viscosity and $\Delta\rho_{\text{lithosphere-mantle}}$ of 65 kg m^{-3} ("reference experiment"). Afterward, we discuss the effect of plate width and mantle viscosity/density ratio.

[37] We scale both toroidal and poloidal mantle velocities by trench velocity v_t, which can be easily measured from the top view.

4.1. Reference Experiment (Experiment 2)

[38] To initiate the process, we manually produce a subduction instability at the tip of the silicone plate by

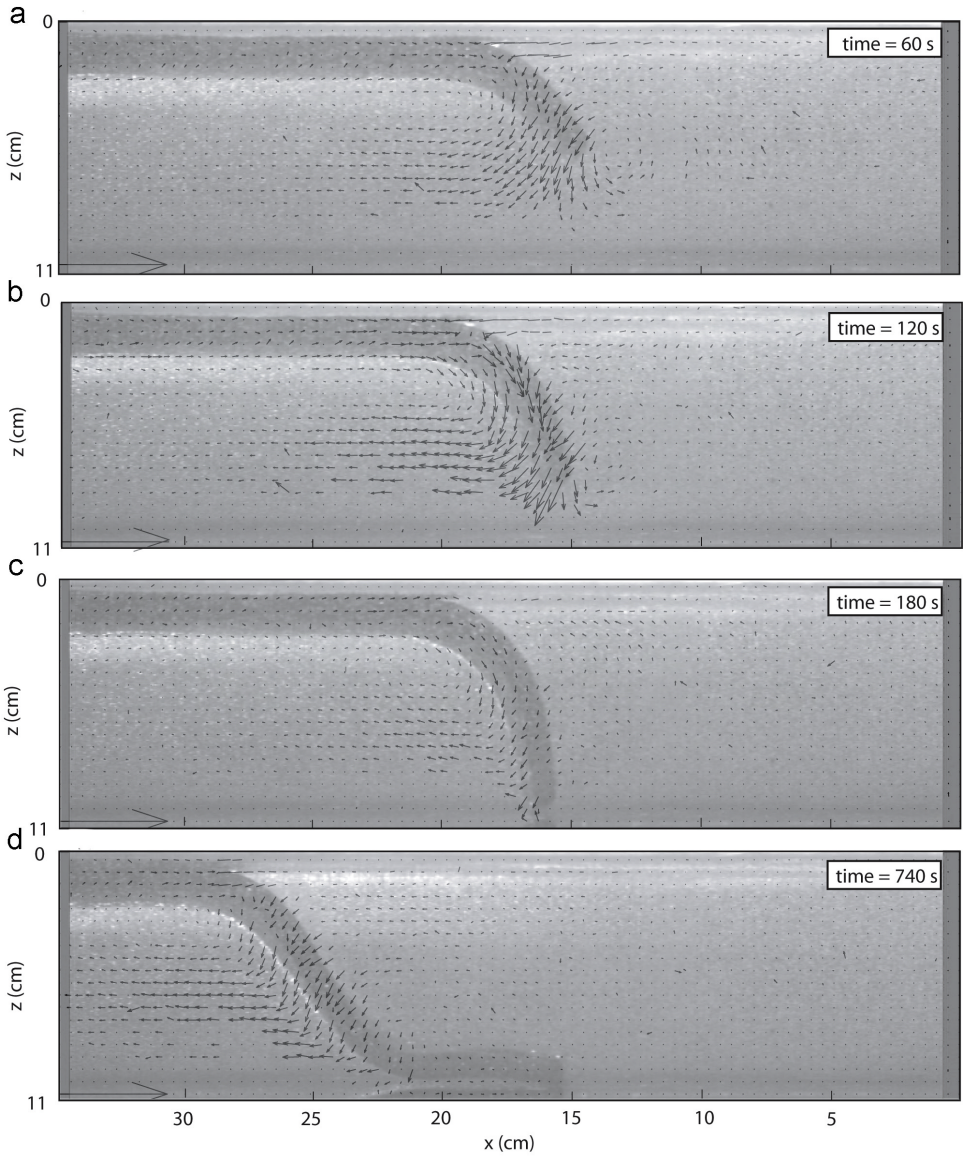

Figure 3. Four selected time steps of ''reference'' experiment 2 showing the time-averaged velocity field recorded in the *x*-*z* section (lateral view) using FT. (a) and (b) First subduction stage (free fall into the upper mantle), (c) second stage (interaction with the 660 km discontinuity), and (d) third stage (steady state subduction regime). FT allows a Lagrangian description of the velocity field providing sparse velocity vectors with application points coincident with tracer particles. Lagrangian data are then used to reconstruct instantaneous and resampling procedure (see section 3 for details). The reference velocity shown at the bottom left corner of each panel is 0.1 cm s^{-1}.

downward bending the slab inside the glucose syrup to a depth of about 3 cm (Figure 1). Then subduction freely evolves, driven by the negative buoyancy of the slab. We observe that the subduction process evolves in three main stages: (1) initial transient sinking into the upper mantle; (2) interaction with 660 km discontinuity; and (3) steady state subduction regime [*Funiciello et al.*, 2003].

4.1.1. Stage 1: Subduction Into the Upper Mantle

[39] At the beginning of experiment the trench retreats progressively accelerating (Figure 2a) and the slab dip increases reaching a maximum angle of about 80° (Figures 3a, 3b and 4). The increase in v_t, resulting from the increase in slab length and the associated slab pull force [*Becker et al.*, 1999], ranges from zero to a maximum of 1.2 cm min^{-1} during subduction into the upper mantle (Figure 2a). The velocity v_{tmax} is reached just before the slab interacts with the bottom of the box, when the negative buoyancy is maximum. Snapshots of mantle circulation for experiment 2 are shown in Figures 3a and 3b and 5a for sections *x*-*z* and *x*-*y*, respectively.

[40] Both poloidal and toroidal advection cells can be recognized in the velocity field pattern since this initial transient stage. FT images show mass exchange of mantle material from the ocean to the wedge side of the plate in

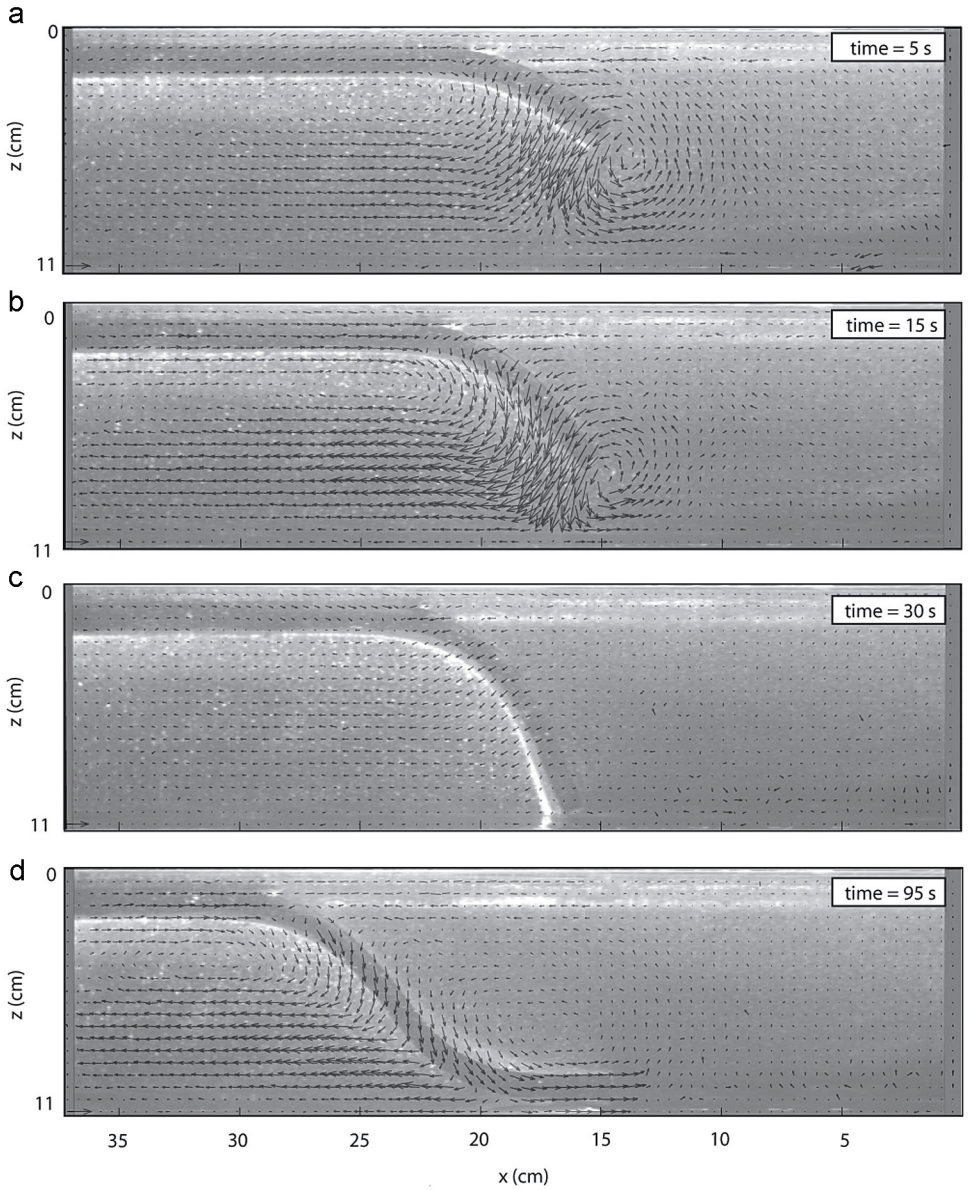

Figure 4. Four selected time steps of experiment 4 showing the time-averaged velocity field recorded in the *x*-*z* section (lateral view) using FT. (a) and (b) First subduction stage, (c) second stage, and (d) third stage. The reference velocity shown at the bottom left corner of each panel is 0.1 cm s^{-1}. For more details see Figure 3.

response to rollback subduction occurring not only around its edges (toroidal circulation) but also underneath the slab tip (poloidal circulation).

[41] In particular, circulation pattern in *x*-*z* section (Figures 3a and 3b) shows two distinct but not isolated cells, one in the ocean and one in the back-arc side, separated by the migrating slab that is an integral part of mantle circulation [*Garfunkel et al.*, 1986]. Different circulation regimes develop within these two cells. The oceanic side cell is wider than the back-arc one and has a shallower and quite stable center compared to the back-arc side cell that migrates progressively toward the bottom of the box following the slab tip. Direction of trajectories in the back-arc cell at shallow depths (3 cm corresponding to 180 km in nature) varies from 0° to 20° from horizontal during the phenomenon evolution. Trajectories close to the slab tip become steeper with time (evolving from 60° to 75° from horizontal) reducing progressively the material exchange between the two circulation cells. Amplitude of velocity vectors reaches up to 50% v_t in the back-arc wedge.

[42] Circulation pattern in the *x*-*y* section (Figure 5a) shows a toroidal cell with mantle circulating around the slab edge. A preliminary set of experiments framing the entire top surface confirmed the symmetry of this velocity pattern with respect to the centerline of the system, showing a toroidal return circulation cell at each side of the plate. Each of the two cells has fixed dimensions (about 50 and 30 cm along *x* and *y* directions, respectively; Figure 5a) and follows the oceanward trench migration. The center of the

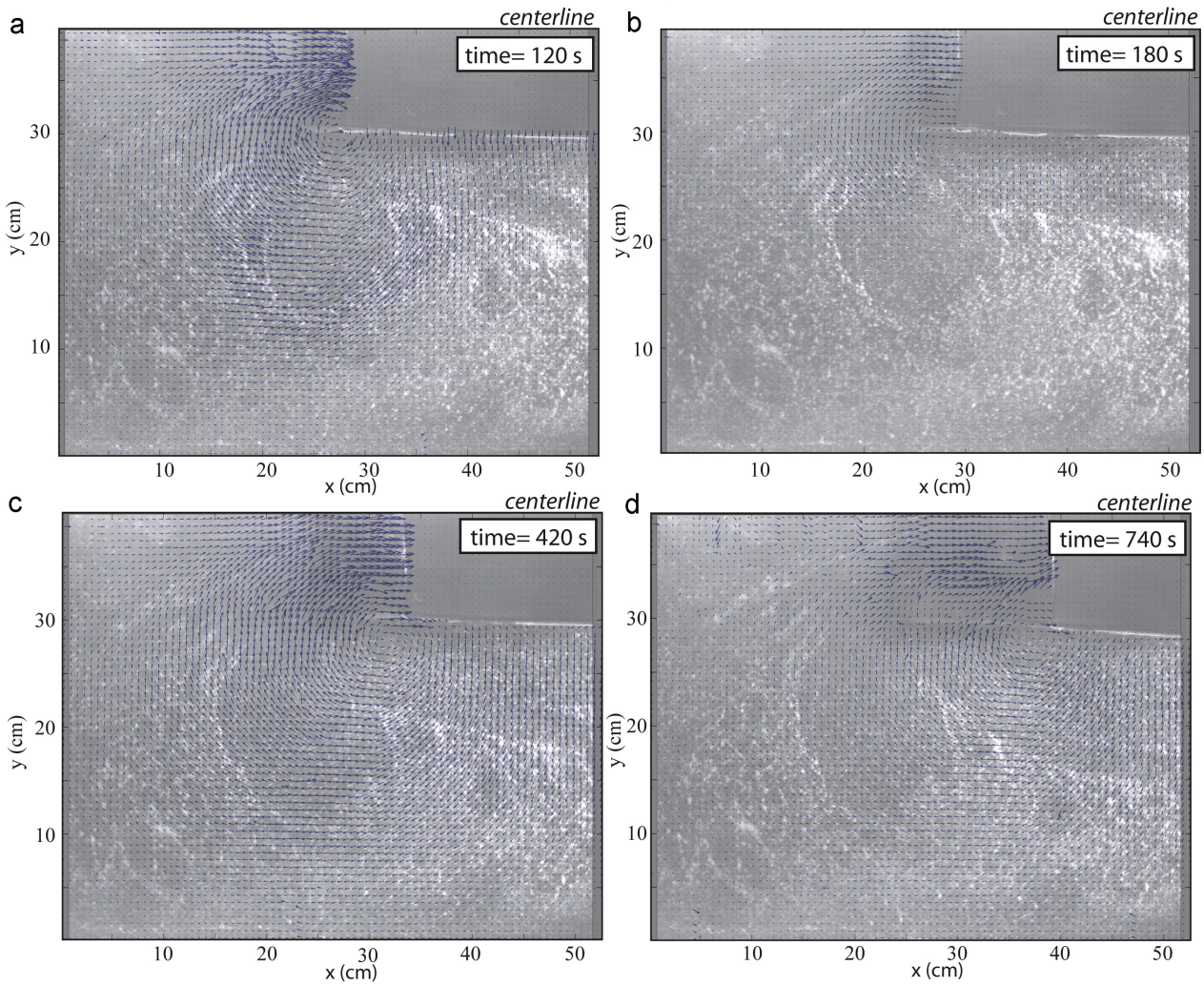

Figure 5. Top view of four time steps for experiment 2 ("reference" experiment) showing the velocity field recorded in the *x*-*y* section. The reference velocity shown on each panel is 0.01 cm/s. Correspondence with subduction stages is the same as for Figure 3.

cell is close to the plate edge. Streamlines of mantle flow have limited interference with lateral box boundaries during the entire evolution of the experiment, confirming the laterally unconstrained character of our experimental setting [*Funiciello et al.*, 2004]. Velocity of the toroidal cell increases with time, consistently with trench velocity reaching its maximum before the slab interacts with the bottom of the box. The peak in mantle velocity is always located in the area in front of the trench, for the whole experiment duration. The maximum mantle velocity achieved during this stage is about 150% v_t.

4.1.2. Stage 2: Interaction With the 660 km Discontinuity

[43] The bottom of the tank is reached after 2′49″ from the beginning of the experiment. In that moment, the trench velocity significantly diminishes (v_t = 0.4 cm min^{-1}) while the tip of the slab folds and deforms in correspondence of the 660 km discontinuity (Figures 2a and 3c). This transient situation pursues for about 1′20″ during which mantle circulation also slows down: poloidal and toroidal mantle velocity components, in fact, considerably decrease (Figures 3c and 5b) and the ocean and back-arc side poloidal cells totally disappear.

4.1.3. Stage 3: Toward a Steady State Regime of Subduction

[44] After the transient stage mantle circulation resumes both in *x*-*z* and *x*-*y* sections till a steady state regime establishes, once the leading edge of the subducting plate has reached a stable arrangement at the bottom of the box (at about 9′). During the steady state regime trench velocity and slab dip keep constant values (Figures 2a, 3d, 5c, and 5d) [see also, e.g., *Funiciello et al.*, 2003]. The steady subduction velocity is the direct consequence of the constant slab pull force applied by the constant portion of subducted lithosphere. The steady state subduction velocity is roughly 1 cm min^{-1} and the slab dip is of about 50° (Figures 2a and 3d).

[45] We observe that poloidal flow restarts in a less vigorous mode than recorded at the end of the first stage (Figure 3d). The ocean and back-arc side cells are both active again, but the oceanic cell is always wider and shallower than the back-arc cell (2.8 cm versus 7.5 cm

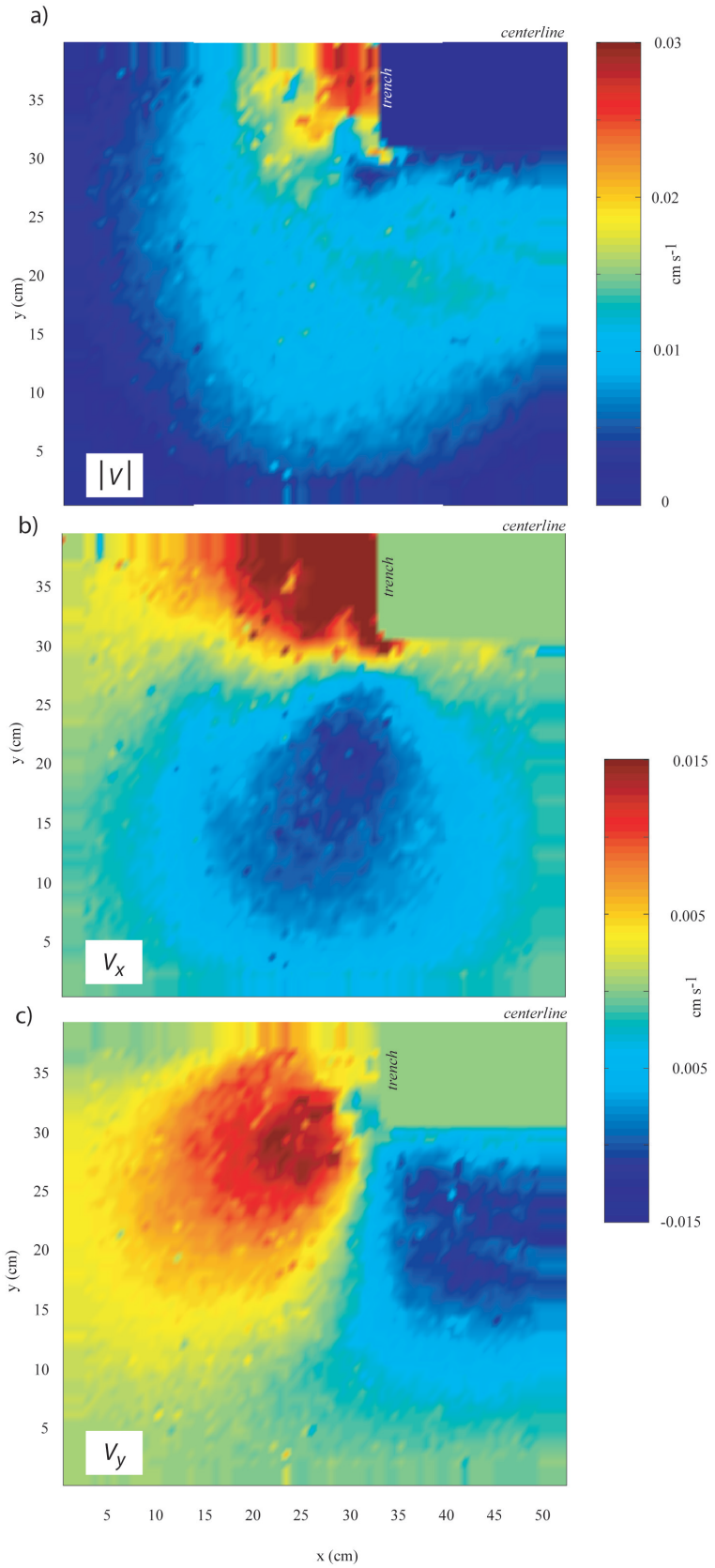

Figure 6. Analysis performed on experiment 2 during the third stage of evolution (t = 420 s). (a) Velocity modulus; (b) x component of velocity; and (c) y component of velocity.

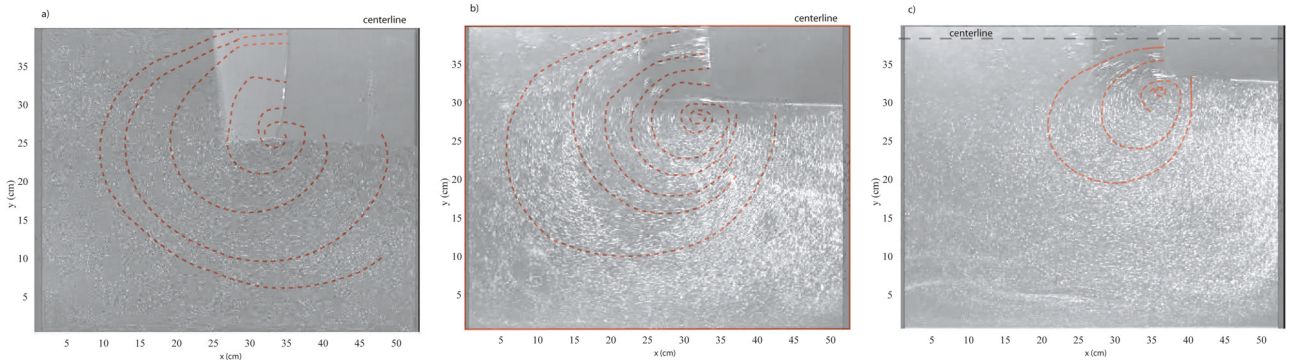

Figure 7. Streamlines of *x*-*y* mantle circulation during the third stage for (a) experiment 1 (520 s), (b) experiment 2 (420 s), and (c) experiment 3 (500 s).

depth). In this stage the slab represents a barrier for material exchange in the vertical direction because it seals the box and mantle circulation from the ocean to the wedge side, due to rollback subduction, occurs now only by means of toroidal advection (Figures 5c, 5d, and 6). Hence toroidal flow becomes an important component of mantle circulation. Each toroidal cell has still a fixed extent in both *x* and *y* directions (about 50 and 30 cm, respectively) (Figures 6 and 7b) and progressively follows the oceanward trench migration. The mantle velocity progressively increases after the slow down produced by the slab-660 km discontinuity interaction. A peak is reached before the leading edge of the subducting plate becomes flat at the bottom of the box (about 7′). Afterward flow velocity assumes steady state values with the maximum rates of 100% v_t recorded in the region in front of the trench.

4.2. Changing Plate Width (Experiments 1, 2, and 3)

[46] In this set of experiments we systematically change the subducting plate width, *w*, preserving laterally unconstrained boundary conditions (see *Funiciello et al.* [2003] for details). Experiments 1 and 3 are similar to the reference experiment, except for *w* which is of 30 and 10 cm, respectively. Trench kinematics for each experiment is illustrated in Figure 2a, while mantle circulation fields are summarized in Figure 8. In order to directly compare all the experiments, we introduce the time-dependent linear absolute flux for both x and y components of the mantle velocity field (Figure 8). Flux components are

$$Q_x = \int |v_y dx| \tag{6}$$

$$Q_y = \int |v_x dy| \tag{7}$$

Q_x (Q_y) is computed integrating the absolute value of v_y (v_x) along the *x* (*y*) direction. Hence it depends on *y* (*x*) and time. For each experiment, Q_x and Q_y are normalized by a reference linear flux obtained multiplying the steady state trench velocity by the plate thickness. To help interpretation, we marked the time of occurrence of the slab-660 km discontinuity interaction, when the mantle circulation temporarily slows down.

[47] General aspects in the evolution of the phenomenon are unchanged with respect to the reference experiment 2: three stages are again recognizable and show the same peculiar characteristics described in detail for the reference experiment both in terms of kinematics of the subducting plate and mantle circulation. As far as mantle circulation is concerned (Figure 8), both Q_x and Q_y show two peaks just before the slab-660 km discontinuity interaction and after the stage 2 is over. Steady state regimes establish afterward, with flux constant through time.

[48] In addition, the role of *w* is fundamental since it strongly influences the subduction process. Here we focus our attention only on the steady state stage, as it is less influenced by initial conditions. As mentioned in the previous section, during this stage the toroidal component largely is enhanced in mantle circulation.

[49] Figure 2 shows that v_t decreases from 1.41 to 1 cm min^{-1}, increasing the plate width from 10 cm to 30 cm, given the viscosity contrast between the lithosphere and the upper mantle characteristic of the experiment. This behavior is in agreement with results obtained by *Bellahsen et al.* [2005] where increasing *w* by three times reduces the trench velocity by 50%. We will show in the next section that this behavior is insensitive to the choice of mantle properties.

[50] The maximum mantle velocity decreases down to v_t by increasing w, but volume of circulating mantle material increases so that the overall mantle flux also increases (Figure 8). In particular, the dimensions of each toroidal cell change from about 30 × 15 cm^2 to about 50 × 35 cm^2 (Figures 7, 8, and 9a) in *x* direction and *y* direction, respectively, as w increases from 10 to 30 cm.

4.3. Changing Mantle Properties (Experiments 4, 5, and 6)

[51] We repeat the previous set of experiments changing the mantle viscosity/density. Experiments 4, 5 and 6 are characterized by a plate width of 30, 20 and 10 cm, respectively, a mantle viscosity of 1 Pa s and a $\Delta\rho_{\text{lithosphere-mantle}}$ of 98 kg m^{-3}. Our choice to decrease mantle viscosity is dictated by the need of preserving laterally unconstrained boundary conditions. The finite box size, in fact, limits our viscosity range, the upper bound being close to the value adopted in the previous experimental set. This appears evident considering that fluid streamlines in experiments 1, 2, and 3 are already quite close to the box sides (Figure 7),

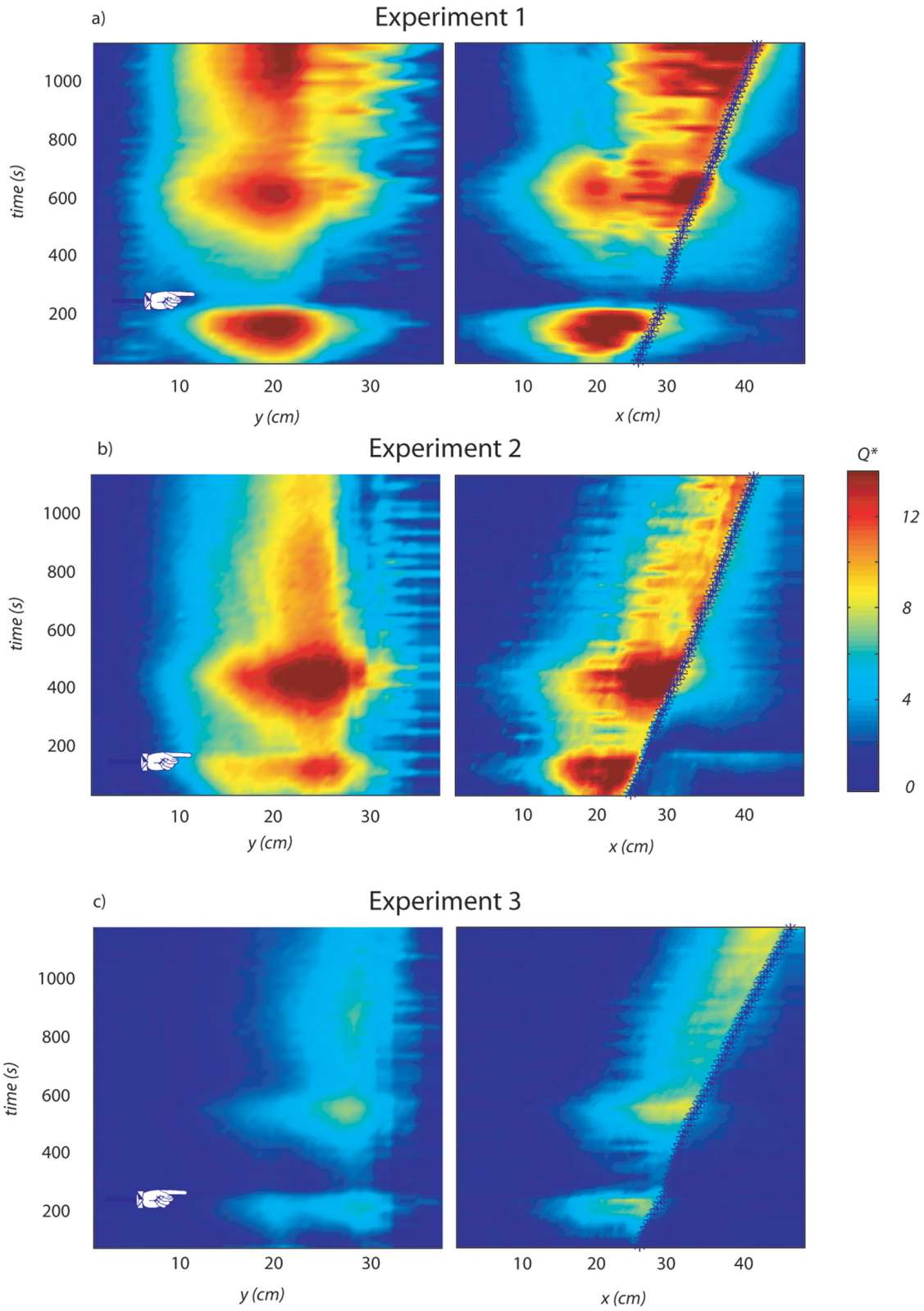

Figure 8. Time evolution of linear flux for both x and y components of mantle circulation for (a) experiment 1, (b) experiment 2, and (c) experiment 3. Flux components are given by $Q_x = \int |v_y dx|$ and $Q_y = \int |v_x dy|$ for each experiment. Both components are normalized by a reference linear flux obtained by multiplying the steady state trench velocity and the plate thickness. For coordinate system, refer to Figure 1. The time when the slab-660 km discontinuity interaction occurs is marked on the left panels. The position of the trench at each time step is indicated by asterisks on the right panels. This figure allows summarizing the evolution of toroidal flow and highlights its main features.

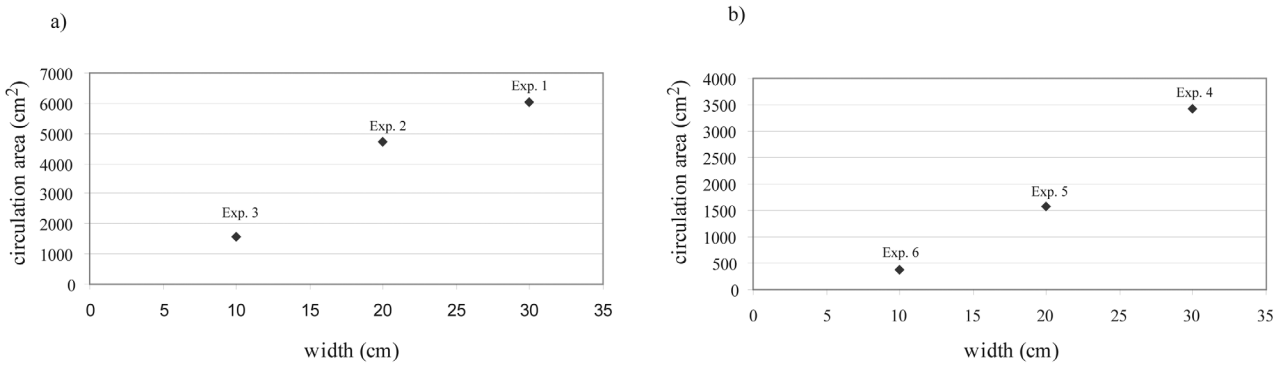

Figure 9. Area affected by subduction induced mantle circulation versus plate width during the third steady state stage for (a) experiments 1, 2, 3 and (b) experiments 4, 5, 6.

meaning that a further increase in viscosity would lead to flow interaction with the box. Trench kinematics for each experiment are illustrated in Figure 2b, while mantle circulation fields are summarized in Figure 10.

[52] Results of this set of experiments are in line with our previous results. The three stages evolution shows the peculiar characteristics described in detail for the reference experiment both in terms of kinematic of subducting plate and of mantle circulation. The key role of the plate width is highlighted again. In particular, the increased viscosity/density ratio between the lithosphere and the underneath mantle speeds up the process by increasing v_t (Figure 2b) and consequently shallowing the slab dip (Figure 4). v_t recorded in the steady state stage is one order of magnitude higher than in the previous set of experiments, about 10 cm min^{-1} on average. Once more v_t decreases with increasing w. This effect is amplified for experiment 6 where for technical needs (i.e., difficulty in positioning a 1.6 cm thick plate over a low viscous fluid) we decreased the plate thickness to 1.1 cm. Mantle circulation gets faster both in x-y and x-z sections (Figure 4). However, the area affected by mantle circulation is smaller than in the previous set of experiments (Figure 9b). A systematic study of the effect of mantle properties in the dynamic of subduction is in progress [*Heuret et al.*, 2005] and will be presented in an upcoming paper.

5. Discussion and Conclusions

[53] Our experiments confirm previous results in terms of subduction kinematics, identifying the presence of a typical sequence of stages in the kinematic evolution of a retreat subduction process, as already described by *Funiciello et al.* [2003, 2004]: the sinking of the slab into the upper mantle; the interaction with the 660 discontinuity; the steady state stage with the slab lying at the upper/lower mantle transition zone. They also confirm the dependency between the plate width and the subduction kinematics [*Funiciello et al.*, 2004; *Bellahsen et al.*, 2005].

[54] The additional outcome of these experiments is to generate images by means of a new detection apparatus (feature tracking) from which we are able to map and to quantitatively estimate the pattern of flow triggered in the mantle by subduction. In this sense, this study is complementary to the one of *Kincaid and Griffiths* [2004], but here the kinematics of the system are dynamically self-consistent and the tracking technique is improved.

[55] Rollback subduction generates a complex 3-D time-dependent circulation pattern characterized by the presence of poloidal and toroidal components, both active since the beginning of the subduction process and evolving according to kinematic stages.

[56] The poloidal component of mantle circulation acts in the x-z plane and results from viscous coupling between the slab and the mantle in answer to the dipward slab motion. As a result, circulation cells are formed in the ocean and in the back-arc sides. Circulation in this plane starts with two cells, one at each side of the migrating slab, characterized by different circulation regimes. The oceanic side is wider than the back-arc side one and has a shallower rotation center, quite stable in depth. Conversely, the back-arc side cell rotation center progressively migrates toward the bottom of the box following the slab tip. Poloidal cells are not separated by the slab and allow return flow beneath the tip of the slab confirming what *Garfunkel et al.* [1986] numerically demonstrated and *Funiciello et al.* [2003, 2004], *Kincaid and Griffiths* [2003] experimentally recognized. *Schellart* [2004a], using the same experimental setup as *Funiciello et al.* [2003, 2004], has qualitatively described the mantle circulation using markers placed inside the mantle concluding that no significant rollback-induced convection underneath the tip of the slab can be observed. In our opinion this discrepancy can be related to the lower accuracy in determining the motion of a limited amount of markers distributed on different x-z planes.

[57] The mantle exchange between the two cells fades away while the slab approaches the 660 km discontinuity. In particular, when the slab interacts with the upper/lower mantle discontinuity, poloidal circulation reduces significantly to be resumed only in the third kinematic stage. In this stage the ocean and back-arc side cells are both active again but the slab obviously represents a barrier for material exchange in the vertical direction.

[58] The toroidal component of mantle circulation, due to the lateral slab migration in presence of lateral viscosity contrast, acts in x-y plane since the first kinematic stage and is characterized by two quasi-symmetrical cells around the slab edges. Each of the two cells keeps fixed dimensions and follows the oceanward trench migration during the

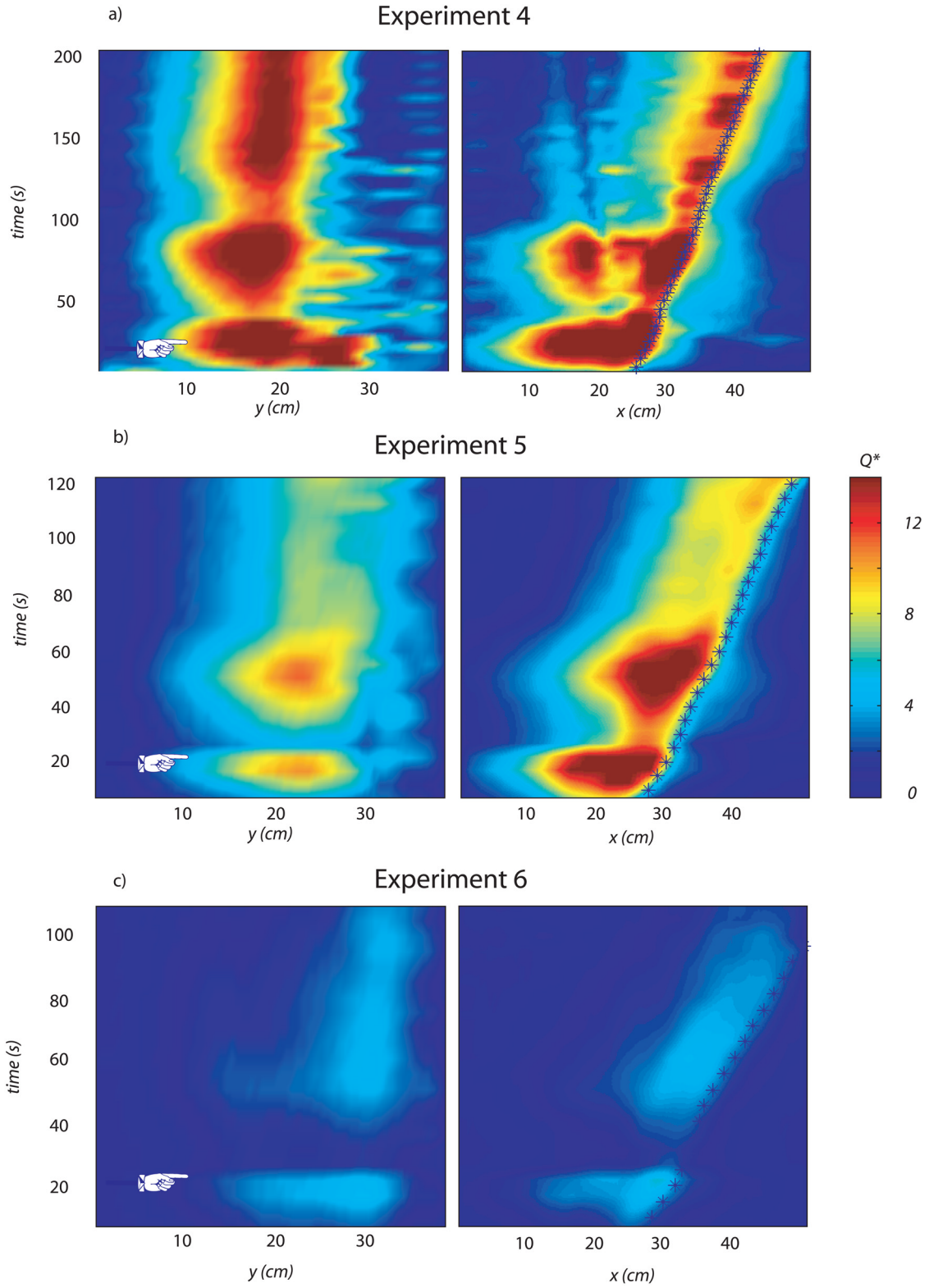

Figure 10. Time evolution of linear flux for both x and y components of mantle circulation for (a) experiment 4, (b) experiment 5, and (c) experiment 6. For more details, see Figure 8.

entire process evolution. The velocity field in the fluid increases with time consistently with trench velocity, reaching a maximum just before the slab interaction with the bottom of the box and attaining the steady state after the slow down caused by the slab interaction with the upper/lower mantle discontinuity. The peak of velocity at each time is recorded in the region in front of the trench, being equal to v_t.

[59] Therefore the transitory kinematic evolution of subduction is reflected into intermittent pulses of toroidal mantle motion particularly vigorous just before and after the interaction between the slab and the 660 km discontinuity (Figures 8 and 10).

[60] Furthermore, these experiments have shown how plate width variations could influence mantle circulation. Increasing w decreases the trench velocity and consequently also mantle velocity decreases. The increase in w also strongly affects the vigor of mantle circulation. In particular, under the same density/viscosity mantle properties, a wider plate moves a larger amount of mantle material (Figure 9).

[61] Comparing this view with circulation models commonly proposed in literature based on the 2-D viscous corner flow approach, we find marked differences. The toroidal component of mantle circulation, missed in those models, assumes a key role modifying the geometry and the efficacy of the poloidal component. In particular, the material resumed at surface from depth in the back-arc wedge is minimal in relation to solutions based on the corner flow theory [*Tovish et al.*, 1978]. The large-scale mass of mantle material flowing around the slab edges could indeed condition the anomalous thermal state of both the slab and mantle wedge [*Currie et al.*, 2004].

[62] **Acknowledgments.** This research is financially supported by ESF-CNR EUROMARGIN research program (WEST-MED, responsible professor Massimo Mattei). The suggestions of an anonymous reviewer and of the Associate Editor improved the quality of this work. Experiments have been performed in the "Laboratory of Experimental Tectonics" Dipartimento Scienze Geologiche Università Roma TRE, Rome, Italy. We are grateful to Syral srl for providing us the sugar syrup used in our experimental models.

References

Adam, J., J. Lohrmann, S. Hoth, N. Kukowski, and O. Oncken (2002), Strain variation and partitioning in thrust wedges: High-resolution data from scaled sandbox experiments by 2D-3D PIV analysis, *Boll. Geofis.*, *42*(1/2), suppl., 123–125.

Adrian, R. J. (1991), Particle imaging techniques for experimental fluid mechanics, *Annu. Rev. Fluid Mech.*, *23*, 261–304.

Barruol, G., and M. Granet (2002), A Tertiary asthenospheric flow beneath the southern French Massif Central indicated by upper mantle seismic anisotropy and related to the west Mediterranean extension, *Earth Planet. Sci. Lett.*, *202*, 31–47.

Becker, T., C. Faccenna, D. Giardini, and R. O'Connell (1999), The development of slabs in the upper mantle: Insights from numerical and laboratory experiments, *J. Geophys. Res.*, *104*, 15,207–15,226.

Bellahsen, N., C. Faccenna, and F. Funiciello (2005), Dynamics of subduction and plate motion in laboratory experiments: Insights into the "plate tectonics" behavior of the Earth, *J. Geophys. Res.*, *110*, B01401, doi:10.1029/2004JB002999.

Ben Ismail, W., and D. Mainprice (1998), An olivine fabric database: An overview of upper mantle fabrics and seismic anisotropy, *Tectonophysics*, *296*, 145–158.

Boffetta, G., M. Cencini, S. Espa, and G. Querzoli (2000), Chaotic advection and relative dispersion in an experimental convective flow, *Phys. Fluids*, *12*, 3160–3167.

Bunge, H. P., M. A. Richards, D. C. Engebretson, and J. R. Baumgardner (1997), A sensitivity study of three-dimensional spherical mantle convection at 108 Rayleigh number: Effects of depth-dependent viscosity, heating mode, and endothermic phase change, *J. Geophys. Res.*, *102*, 11,991–12,007.

Buttles, J., and P. Olson (1998), A laboratory model of subduction zone anisotropy, *Earth Planet. Sci. Lett.*, *164*(1–2), 245–262.

Christensen, U. R. (1996), The influence of trench migration on slab penetration into the lower mantle, *Earth Planet. Sci. Lett.*, *140*, 27–39.

Cloos, M. (1993), Lithospheric buoyancy and collisional orogenesis: Subduction of oceanic plateaus, continental margins, island arcs, spreading ridges, and seamounts, *Geol. Soc. Am. Bull.*, *105*(6), 715–737.

Conder, J. A., D. A. Wiens, and J. Morris (2002), On the decompression melting structure at volcanic arcs and back-arc spreading centers, *Geophys. Res. Lett.*, *29*(15), 1727, doi:10.1029/2002GL015390.

Conrad, C. P., and B. H. Hager (1999), Effects of plate bending and fault strength at subduction zones on plate dynamics, *J. Geophys. Res.*, *104*, 17,551–17,571.

Currie, C. A., K. Wang, R. D. Hyndman, and J. He (2004), The thermal effects of slab-driven mantle flow above a subducting plate: The Cascadia subduction zone and backarc, *Earth Planet. Sci. Lett.*, *223*, 35–48, doi:10.1016/j.epsl.2004.04.020.

Davaille, A., M. Le Bars, and C. Carbonne (2003), Thermal convection in a heterogeneous mantle, *C. R. Geosci.*, *335*(1), 141–156.

Davies, G. F. (1995), Penetration of plates and plumes through the mantle transition zone, *Earth Planetary Sci. Lett.*, *133*, 507–516.

Davies, J. H., and D. J. Stevenson (1992), Physical model of source region of subduction zone Volcanics, *J. Geophys. Res.*, *97*, 2037–2070.

Davy, P., and P. R. Cobbold (1991), Experiments of a 4-layer continental lithosphere, *Tectonophysics*, *188*, 1–25.

Di Florio, D., F. Di Felice, and G. P. Romano (2002), Windowing, reshaping and re-orientation interrogation windows in particle image velocimetry for the investigation of shear flows, *Meas. Sci. Technol.*, *13*, 953–962.

Eberle, M. A., O. Grasset, and C. Sotin (2002), A numerical study of the interaction between the mantle wedge, subducting slab and over-riding plate, *Phys. Earth Planet. Inter.*, *134*, 191–202.

Faccenna, C., D. Giardini, P. Davy, and A. Argentieri (1999), Initiation of subduction at Atlantic-type margins: Insights from laboratory experiments, *J. Geophys. Res.*, *104*, 2749–2766.

Faccenna, C., C. Piromallo, A. Crespo-Blanc, L. Jolivet, and F. Rossetti (2004), Lateral slab deformation and the origin of the western Mediterranean arcs, *Tectonics*, *23*, TC1012, doi:10.1029/2002TC001488.

Fischer, K. M., E. M. Parmentier, A. R. Stine, and E. R. Wolf (2000), Modeling anisotropy and plate-driven flow in the Tonga subduction zone back arc, *J. Geophys. Res.*, *105*, 16,181–16,191.

Funiciello, F., C. Faccenna, D. Giardini, and K. Regenauer-Lieb (2003), Dynamics of retreating slabs: 2. Insights from three-dimensional laboratory experiments, *J. Geophys. Res.*, *108*(B4), 2207, doi:10.1029/2001JB000896.

Funiciello, F., C. Faccenna, and D. Giardini (2004), Role of lateral mantle flow in the evolution of subduction system: Insights from 3-D laboratory experiments, *Geophys. J. Int.*, *157*, 1393–1406.

Garfunkel, Z., D. L. Anderson, and G. Schubert (1986), Mantle circulation and lateral migration of subducting slabs, *J. Geophys. Res.*, *91*, 7205–7223.

Giardini, D., and J. H. Woodhouse (1984), Deep seismicity and modes of deformation in Tonga subduction zone, *Nature*, *307*, 505–509.

Grand, S. P., R. D. van der Hilst, and S. Widiyantoro (1997), Global seismic tomography: A snapshot of convection in the Earth, *GSA Today*, *7*, 1–17.

Griffiths, R. W., and J. S. Turner (1988), Folding of viscous plumes impinging on a density or viscosity interface, *Geophys. J.*, *95*, 397–419.

Griffiths, R. W., R. I. Hackney, and R. D. van der Hilst (1995), A laboratory investigation of effects of trench migration on the descent of subducted slabs, *Earth Planet. Sci. Lett.*, *133*(1–2), 1–17.

Guillou-Frottier, L., J. Buttles, and P. Olson (1995), Laboratory experiments on structure of subducted lithosphere, *Earth Planet. Sci. Lett.*, *133*, 19–34.

Hampel, A., N. Kukowski, J. Adam, and C. Huebscher (2003), The subduction of the Nazca Ridge at the Peruvian margin: Insights into the mass transfer regime from geophysical data and a PIV-monitored 3-D sandbox experiment, *Geophys. Res. Abstr.*, *5*, Abstract 05866.

Heuret, A., and S. Lallemand (2004), Plate motions, slab dynamics and back-arc deformation, *Phys. Earth Planet. Inter.*, *149*(1–2), 31–51.

Heuret, A., F. Funiciello, C. Faccenna, and S. Lallemand (2005), Insights into the dynamics of subduction from statistical observations and laboratory experiments, paper presented at European Geoscience Union, Vienna.

Iidaka, T., and F. Niu (2001), Seismic anisotropy beneath the Lau back-arc basin inferred from sScS-ScsS splitting data, *Geophys. Res. Lett.*, *28*, 863–866.

Isacks, B. L., and M. Barazangi (1977), Geometry of Benioff zone: Lateral segmentation and downwards bending of the subducted lithosphere, in *Island Arcs, Deep Sea Trenches, and Back-Arc Basins*, *Maurice Ewing Ser.*, vol. 1, edited by M. Talwani and W. C. Pitman, pp. 99–114, AGU, Washington D. C.

Jarrard, R. D. (1986), Relations among subduction parameters, *Rev. Geophys.*, *24*, 217–284.

Kincaid, C., and R. W. Griffiths (2003), Laboratory models of the thermal evolution of the mantle during rollback subduction, *Nature*, *425*, 58–62.

Kincaid, C., and R. W. Griffiths (2004), Variability in flow and temperatures within mantle subduction zones, *Geochem. Geophys. Geosyst.*, *5*, Q06002, doi:10.1029/2003GC000666.

Kincaid, C., and P. S. Hall (2003), Role of back arc spreading in circulation and melting at subduction zones, *J. Geophys. Res.*, *108*(B5), 2240, doi:10.1029/2001JB001174.

Kincaid, C., and P. Olson (1987), An experimental study of subduction and slab migration, *J. Geophys. Res.*, *92*, 13,832–13,840.

Kincaid, C., and I. S. Sacks (1997), Thermal and dynamical evolution of the upper mantle in subduction zones, *J. Geophys. Res.*, *102*, 12,295–12,315.

King, S. D., and B. H. Hager (1990), The relationship between plate velocity and trench viscosity in Newtonian and power-law subduction calculations, *Geophys. Res. Lett.*, *17*, 2409–2412.

King, S. D., and B. H. Hager (1994), Subducted slabs and the geoid: 1. Numerical experiments with temperature-dependent viscosity, *J. Geophys. Res.*, *99*, 19,843–19,852.

Kumagai, I., T. Yanagisawa, and K. Kurita (2003), Importance of entrainment in mantle plume dynamics, paper presented at European Geophysical Society Meeting 2003, Nice, France.

Lithgow-Bertelloni, C., and M. A. Richards (1998), The dynamics of Cenozoic and Mesozoic plate motions, *Rev. Geophys.*, *36*, 27–78.

Miozzi, M. (2004), Particle image velocimetry using feature tracking and Delauny tessellation, paper presented at 12th International Symposium on Application of Laser Techniques to Fluid Mechanics, Inst. Super. Tecn., Lisbon.

Molnar, P., and D. Gray (1979), Subduction of continental lithosphere: Some constraints and uncertainties, *Geology*, *7*, 58–62.

Montagner, J. P., and L. Guillot (2000), Seismic anisotropy in the Earth's mantle, in *Problems in Geophysics for the Next Millenium*, edited by E. Boschi, G. Ekström, and A. Morelli, pp. 217–254, Ist. Naz. di Geofis. e Vulcanol., Erice, Italy.

Moroni, M., and A. Cenedese (2006), Comparison among Feature tracking and more consolidated velocimetry image analysis techniques in a fully developed turbulent channel flow, *Meas. Sci. Technol.*, in press.

Moroni, M., and J. H. Cushman (2001), Three-dimensional particle tracking velocimetry studies of the transition from pore dispersion to Fickian dispersion for homogeneous porous media, *Water Resour. Res.*, *37*(4), 873–884.

Nakajima, J., and A. Hasegawa (2004), Shear-wave polarization anisotropy and subduction-induced flow in the mantle wedge of northeastern Japan, *Earth Planet. Sci. Lett.*, *225*, 365–377.

Nogueira, J., A. Leucona, and P. A. Rodriguez (2001), Local field correction PIV implemented by means of simples algorithms, and multigrid versions, *Meas. Sci. Technol.*, *12*, 1911–1921.

Olbertz, D., M. J. R. Wortel, and U. Hansen (1997), Trench migration and subduction zone geometry, *Geophys. Res. Lett.*, *24*, 221–224.

Pearce, J. A., P. T. Leat, P. F. Bearker, and I. L. Millar (2001), Geochemical tracing of Pacific to Atlantic upper-mantle flow through the Drake passage, *Nature*, *410*, 457–461.

Peyton, V., V. Levin, J. Park, M. T. Brandon, J. Lees, E. Gordeev, and A. Ozerov (2001), Mantle flow at a slab edge: Seismic anisotropy in the Kamchatka region, *Geophys. Res. Lett.*, *28*, 379–382.

Ranalli, G. (1995), *Rheology of the Earth*, 413 pp., CRC Press, Boca Raton, Fla.

Ricard, Y., C. Doglioni, and R. Sabadini (1991), Differential rotation between lithosphere and mantle: A consequence of lateral mantle viscosity variations, *J. Geophys. Res.*, *96*, 8407–8415.

Russo, R. M., and P. G. Silver (1994), Trench-parallel flow beneath the Nazca plate from seismic anisotropy, *Science*, *263*, 1105–1111.

Savage, M. K. (1999), Seismic anisotropy and mantle deformation: What have we learned from shear wave splitting?, *Rev. Geophys.*, *37*, 69–106.

Schellart, W. P. (2004a), Kinematics of subduction and subduction-induced flow in the upper mantle, *J. Geophys. Res.*, *109*, B07401, doi:10.1029/2004JB002970.

Schellart, W. P. (2004b), Quantifying the net slab pull force as a driving mechanism for plate tectonics, *Geophys. Res. Lett.*, *31*, L07611, doi:10.1029/2004GL019528.

Shemenda, A. I. (1992), Horizontal lithosphere compression and subduction: Constraints provided by physical modeling, *J. Geophys. Res.*, *97*, 1097–1116.

Silver, P. G., and W. W. Chan (1991), Shear wave splitting and subcontinental deformation, *J. Geophys. Res.*, *96*, 16,429–16,454.

Smith, G. P., D. A. Wiens, K. M. Fischer, L. M. Dorman, S. C. Webb, and J. A. Hildebrand (2001), A complex pattern of mantle flow in the Lau backarc, *Science*, *292*, 713–716.

Tackley, P. J. (2000a), Self-consistent generation of tectonic plates in time-dependent, three-dimensional mantle convection simulations, *Geochem. Geophys. Geosyst.*, *1*(8), doi:10.1029/2000GC000036.

Tackley, P. J. (2000b), Self-consistent generation of tectonic plates in time-dependent, three-dimensional mantle convection simulations, *Geochem. Geophys. Geosyst.*, *1*(8), doi:10.1029/2000GC000043.

Tetzlaff, M., and H. Schmeling (2000), The influence of olivine metastability on deep subduction of oceanic lithosphere, *Phys. Earth Planet. Inter.*, *120*, 29–38.

Tichelaar, B. W., and L. J. Ruff (1993), Depth of seismic coupling along subduction zones, *J. Geophys. Res.*, *98*, 2017–2037.

Tovish, A., G. Schubert, and B. P. Luyendyk (1978), Mantle flow pressure and the angle of subduction: Non-Newtonian corner flows, *J. Geophys. Res.*, *83*, 5892–5898.

Turcotte, D. L., and G. Schubert (1982), *Geodynamics Application of Continuum Physics to Geological Problems*, 450 pp., John Wiley, Hoboken, N. J.

Turner, S., and C. J. Hawkesworth (1998), Using geochemistry to map mantle flow beneath the Lau basin, *Geology*, *26*, 1019–1022.

Weijermars, R., and H. Schmeling (1986), Scaling of Newtonian and non-Newtonian fluid dynamics without inertia for quantitative modelling of rock flow due to gravity (including the concept of rheological similarity), *Phys. Earth Planet. Inter.*, *43*, 316–330.

Wendt, J. I., M. Regelous, K. D. Collerson, and A. Ewart (1997), Evidence for a contribution from two mantle plumes to island-arc lavas from northern Tonga, *Geology*, *25*, 611–614.

Wortel, R. (1982), Seismicity and rheology of subducted slabs, *Nature*, *296*, 553–556.

Yang, X. P., K. M. Fischer, and G. A. Abers (1995), Seismic anisotropy beneath the Shumagin Islands segment of the Aleutian-Alaska subduction zone, *J. Geophys. Res.*, *100*, 18,165–18,177.

Zhong, S., and M. Gurnis (1994), Role of plates and temperature-dependent viscosity in phase-change dynamics, *J. Geophys. Res.*, *99*, 15,903–15,917.

Zhong, S., M. Gurnis, and L. Moresi (1998), Role of faults, nonlinear rheology, and viscosity structure in generating plates from instantaneous mantle flow models, *J. Geophys. Res.*, *103*, 15,255–15,268.

H. A. Bui, C. Faccenna, and F. Funiciello, Dipartimento di Scienze Geologiche, Università degli Studi "Roma TRE," L.go S.L. Murialdo 1, I-00146 Rome, Italy. (ffunicie@uniroma3.it)

A. Cenedese and M. Moroni, Dipartimento di Idraulica, Trasporti e Strade, Università degli Studi di Roma "La Sapienza", Via Eudossiana, 18, I-00184 Rome, Italy.

C. Piromallo, Istituto Nazionale di Geofisica e Vulcanologia, Via di Vigna Murata 605, I-00143 Rome, Italy.